Modeling Bidirectional Contactless Grid Interfaces With a Soft DC-Link

Saranga Weearsinghe, *Student Member, IEEE*, Duleepa J. Thrimawithana, *Member, IEEE*, and Udaya K. Madawala, *Senior Member, IEEE*

***Abstract*—Inductively coupled, bidirectional grid interfaces are gaining popularity as an attractive solution for vehicle-to-grid (V2G) and grid-to-vehicle (G2V) systems. However, such systems conventionally employ a large, electrolytic dc-link capacitor as well as a large input inductor, leading to expensive, bulky, and less reliable systems. Although, matrix converter (MC) based bidirectional inductive power transfer (BD-IPT) grid interfaces have been proposed as an alternative, implementation of safe and reliable MCs in BD-IPT applications is still a challenge, owing to the absence of natural freewheeling paths and higher complexity. As a solution, this paper proposes a new, inductively coupled, bidirectional grid interface, without a dc-link capacitor and an input inductor, consisting of two back-to-back connected converters. In contrast to existing bidirectional grid converters, the proposed system employs a simpler switching strategy with a lower switching frequency. A mathematical model, which predicts the behavior of the introduced system, is also presented. The feasibility of the proposed technique and the accuracy of the mathematical model are demonstrated through both simulations and experimental results of a 1.1-kW prototype system.**

***Index Terms*—DC-link capacitor, electric vehicles (EVs), grid converters, inductive power transfer (IPT), matrix converters (MCs).**

I. Introduction

In recent years, the demand for electric vehicles (EVs) has risen significantly due to several reasons, such as improvement in EV technologies, high fuel costs associated with conventional vehicles, and increased awareness on reducing greenhouse gas emissions. Moreover, with the emergence of vehicle-to-grid (V2G) and grid-to-vehicle (G2V) technologies, EVs have been proposed as energy storage devices for storage and retrieval of energy for dynamic demand management [1]–[3].

Currently, hard-wired bidirectional grid interfaces are employed for grid integration of EVs. Although hard-wired interfaces between EVs and the utility grid are simple, they must be suitably isolated to avoid the risk of shock hazards [4]. However, they still increase the risk of electrocution, particularly under wet environments and harsh weather conditions, such as snow and ice, making safe use of hard-wired interfaces practically difficult. Since these particular grid interfaces are equipped with long cables, they can also be inconvenient and inflexible [5]. In recent years, inductive power transfer (IPT) has emerged as a favored technique for supplying contactless power for a wide range of applications [6]–[12]. In contrast to hardwired interfaces, contactless grid interfaces based on bidirectional inductive power transfer (BD-IPT) technology have shown substantial promise as an attractive solution for V2G and G2V applications due to their higher galvanic isolation, flexibility, and efficiencies comparable to hard-wired systems [9]. Nevertheless, the operating frequencies of BD-IPT systems are typically much higher than the utility grid frequency. Therefore, contactless grid integration of EVs for V2G or G2V applications involves a single or multistage frequency conversion, using one or more bidirectional power electronic converters. Furthermore, as a typical BD-IPT system includes a sixth or eighth order, high-frequency resonant network [13], control of such systems is more demanding in contrast to traditional applications. Nonetheless, two different types of bidirectional converter topologies that are used for grid integration of BD-IPT systems have been reported in the literature [14], [15].

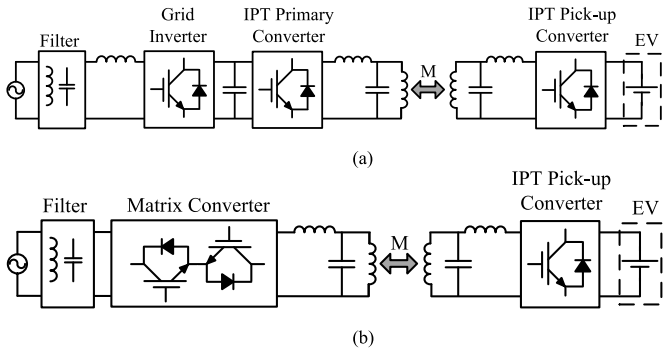

Fig. 1. Converter topologies for grid integration of BD-IPT systems (a) grid inverter-based system (b) MC-based system.

Out ofthe two topologies reported, one that is reported in [14] consists of a two-stage energy conversion process, using two converters on the primary side of the BD-IPT system, as shown in Fig. 1(a). The converter on the front end, which is referred to as the grid inverter, is driven by high-frequency PWM signals based on proportional-resonant or direct-quadrature controllers. By doing so, it converts the utility grid ac voltage to a dc voltage and maintains the converted dc voltage at a relatively constant value. The converter on the back end, known as the IPT primary converter, then converts the constant dc voltage at the intermediate dc-link to an ac voltage at the resonant frequency, in order to drive the resonant network. Hence, this system necessitates a large electrolytic dc-link capacitor and an input inductor

Manuscript received March 16, 2014; revised June 7, 2014; accepted July 27, 2014. Date of publication August 12, 2014; date of current version February 13, 2015. Recommended for publication by Associate Editor M. Liserre.

The authors are with the Department of Electrical and Computer Engineering, The University of Auckland, Auckland 1010, New Zealand (e-mail: s.weerasinghe@auckland.ac.nz; d.thrimawithana@auckland.ac.nz; u.madawala@auckland.ac.nz).

Color versions of one or more of the figures in this paper are available online at http://ieeexplore.ieee.org.

Digital Object Identifier 10.1109/TPEL.2014.2347038

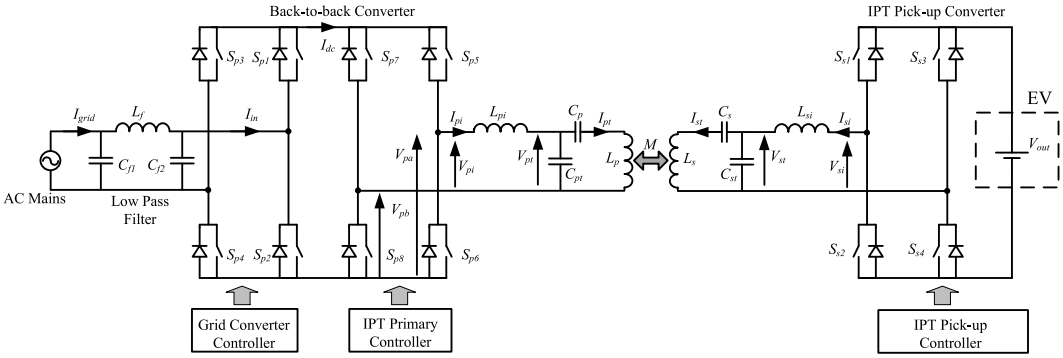

Fig. 2. Proposed converter topology for grid integration of BD-IPT systems.

for minimizing voltage ripple at the intermediate dc-link and reducing input current ripples, respectively. Inclusion of these two energy storage elements makes the system bulky and more expensive. In addition, numerous external factors such as, type of dielectric material used, operating and storage temperatures, contribute to determining the life time of the dc-link capacitor [16], [17]. As a result, inclusion of the dc-link capacitor compromises the reliability of the entire system [18].

Alternately, matrix converter (MC)-based bidirectional inductively coupled grid interfaces have been proposed in [15]. Being a direct ac–ac converter, the MC is able to convert low-frequency ac voltage on the grid side to a high-frequency ac voltage at the converter output. Consequently, this eliminates the requirement of a large input inductor, dc-link capacitor, and the additional ac–dc conversion stage in the grid inverter-based system as shown in Fig. 1(b). Hence, the MC-based system becomes less expensive and more compact in comparison to a conventional grid inverter-based system. However, current commutation of the MC must be controlled using precise and complex multistep commutation algorithms [19]–[21]. Thus, the complexity of the controller of the MC-based system becomes significantly higher, particularly in BD-IPT applications where high frequency, high-order resonant networks are present. Hence, reliable and safe operation of the MC is very demanding.

This paper presents an inductively coupled, bidirectional grid interface scheme that overcomes aforementioned drawbacks of existing systems. The proposed system performs two-stage energy conversion using two converters, without having a constant or stiff dc-link voltage. Therefore, it eliminates the need of a large dc-link capacitor. Owing to the absence of the dc-link capacitor, a voltage with a large ripple, which is close to the peak of the grid voltage, is manifested in the dc-link voltage of the proposed system. Hence, the dc-link of the proposed system is referred to as soft dc-link in this paper. The large input inductor has also been excluded by exploiting the inherent current source nature [9] of the parallel resonant circuit. This attributes to a more compact, reliable, and a less expensive system in comparison to conventional grid inverter-based systems. Moreover, in contrast to the existing systems, the front end converter can be operated using a simple switching strategy at utility grid frequency, with near-zero-voltage switching. The paper presents comprehensive mathematical analyses and compares theoretical results with those obtained from a 1.1-kW experimental prototype and a MATLAB simulation model to demonstrate system's capability to realize regulated bidirectional power flow to/from the grid. Furthermore, the total harmonic distortion (THD) of the grid current, power factor, and the efficiency of the overall system are presented to investigate the performance of the proposed scheme. Results suggest that the proposed bidirectional inductively coupled grid interface is efficient, reliable, and easy to implement, and suitable for contactless V2G and G2V applications.

II. Proposed Grid-Integrated Bidirectional IPT System

A schematic of the proposed grid integrated BD-IPT system is shown in Fig. 2. The primary side of the system consists of two converters that are connected in a back-to-back configuration. The front end converter, which is referred to as the grid converter, is directly interfaced with the utility grid. Due to current source nature of the tuned inductor–capacitor–capacitor–inductor (*LCCL*) resonant network [13], an input inductor is not required for controlling the grid current. Therefore, the large input inductor is eliminated. Regardless of the direction of the power flow, switching devices S_{p1} and S_{p4} remain ON during the entire positive half of the grid voltage, whereas, during the negative half cycle of the grid voltage S_{p2} and S_{p3} remain ON. However, this requires precise detection of zero-voltage crossings of the utility grid voltage, but measuring voltages accurately near zero is practically a difficult task. To make the situation worse, incorrect detection of zero-voltage crossings can lead to a phase-to-neutral short circuit through the grid converter. Hence, safe and reliable operation of the grid converter is performed based on two voltage limits, $\triangle V+$ and $\triangle V-$, which are slightly above and below zero of the utility grid voltage, respectively. When the grid voltage is within $\triangle V+$ and $\triangle V-$, a deadband, during which $S_{p1} - S_{p4}$ are turned OFF as shown in Fig. 3, is introduced. Thus, the utility grid supply is completely disconnected from the BD-IPT system, during the deadband. When the grid voltage, $V_{\rm grid} > \triangle V+$ and $V_{\rm grid} < \triangle V-$, the grid converter is said to be in normal operation. Due to the switching of $S_{p1} - S_{p4}$ as shown in Fig. 3, a dc voltage with a ripple of $V_{\rm in}$ is formed in the dc-link, where $V_{\rm in}$ is the peak of the utility grid voltage. Thus, the grid converter functions as a rectifier at

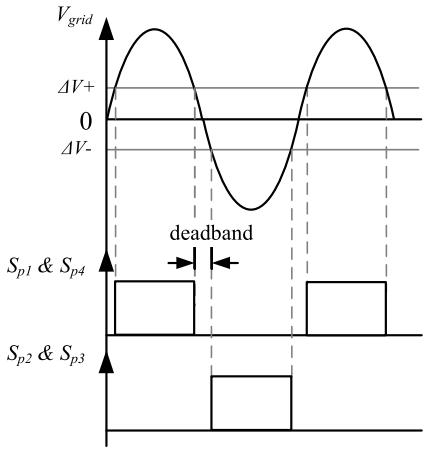

Fig. 3. Operation of $S_{p1} - S_{p4}$ with deadband.

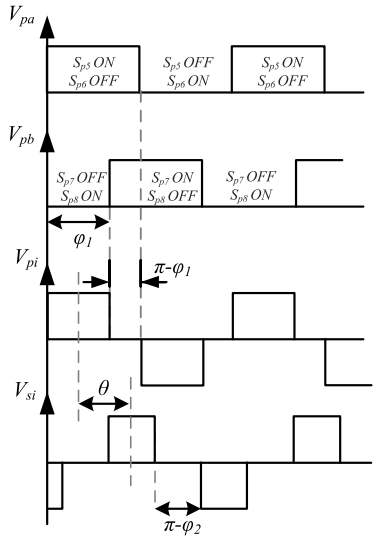

Fig. 4. Voltages produced by IPT primary and pick-up converters.

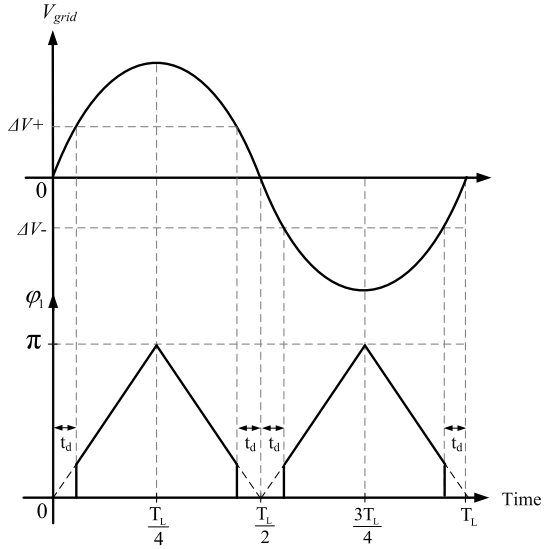

Fig. 5. Regulation of primary phase modulation φ_1 with grid voltage.

utility grid frequency when the power flows from the grid to the EV, while it operates as an inverter when the power flow is in reverse direction, i.e., from the EV to the grid.

The IPT primary converter in Fig. 2 is employed for converting the dc voltage across the soft dc-link into an ac voltage at resonant frequency. Switching devices S_{p5} and S_{p6} of the IPT primary converter are switched at the resonant frequency f_T, with a duty cycle of 50%, to generate a square wave voltage V_{pa} as shown in Fig. 4. In order to generate V_{pb}, S_{p7}, and S_{p8} are operated at f_T with a 50% duty cycle but with a phase delay φ_1 with respect to V_{pa}, which is referred to as the primary phase modulation. Due to the difference between V_{pa} and V_{pb}, an ac voltage V_{pi} at f_T manifests at the output of the primary IPT converter, and the effective value of V_{pi} depends on the primary phase modulation. Subsequently, V_{pi} produces a current I_{pt} in the primary winding L_p which is loosely coupled to the pick-up winding L_s. The IPT pick-up converter in Fig. 2 is also operated using the same principle, but with a relative phase shift θ with respect to V_{pi}, as illustrated in Fig. 4. This converts the dc voltage $V_{\rm out}$, which represents an EV for simplicity, to an ac voltage V_{si} at the same resonant frequency f_T. As a result, a current I_{st} in the pick-up winding L_s is generated. Contactless power transfer takes place across the air gap between the primary and the pick-up windings due to the mutual coupling between them, and the relative phase angle between I_{pt} and I_{st}, which essentially depends on θ, determines the magnitude and direction of power flow. In order to maintain the power factor of the system near unity, the relative phase angle θ is maintained at $\pm 90^\circ$ [9], and hence, the regulation of power is accomplished by controlling the pick-up phase modulation φ_2.

Furthermore, as the grid converter disconnects the BD-IPT system from the utility grid during the deadband, it is essential for the primary IPT converter to interrupt the flow of energy from/to the soft dc-link to prevent an undershoot or overshoot of the soft dc-link voltage during this particular time frame. Therefore, the primary phase modulation φ_1 is retained at 0° and, consequently, the IPT primary converter short circuits the primary *LCCL* resonant network to decouple it from the pick-up. Hence, no power transfer takes place between the primary and the pick-up systems during the deadband. In order to reduce grid current THD, the technique reported in [22] for MC-based grid connected BD-IPT systems, has been adopted in the proposed back-to-back converter (BTBC)-based BD-IPT system. This technique basically modulates I_{pi} by controlling primary phase modulation φ_1, so that grid current $I_{\rm grid}$ gets modulated. For that reason, φ_1 is linearly regulated with the phase of $V_{\rm grid}$ as shown in Fig. 5, where t_d represents the duration of the deadband, and $V_{\rm grid} = V_{\rm in}\sin(\omega_L t)$. Moreover, to prevent the injection of high-frequency harmonic currents to the grid, a small low-pass filter as shown in Fig. 2 was employed between the grid converter and the utility grid.

III. Mathematical Model

Due to the operation of the grid converter, a dc voltage of $V_{\rm in}\,|\sin(\omega_L t)|$ is produced across the soft dc-link, where ω_L

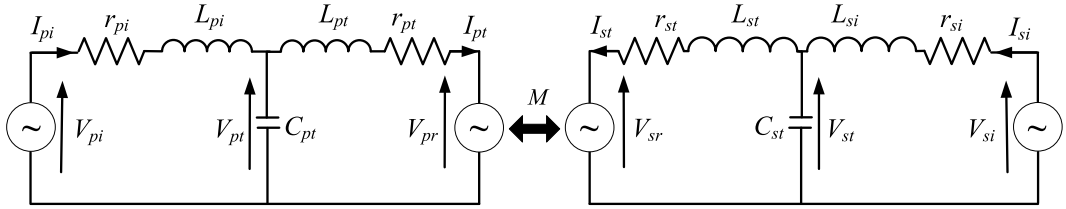

Fig. 6. Reduced *LCL* network.

represents the frequency of the utility grid voltage. Hence, the IPT primary converter produces an ac voltage at its output, which can be given by

$$V_{pi} = V_{\text{in}} \left|\sin(\omega_L t)\right| \frac{4}{\pi} \sum_{n=1,3\ldots}^{\infty} \frac{1}{n} \cos(n\omega_T t) \sin\left(\frac{n\varphi_1}{2}\right) \quad (1)$$

where ω_T is the angular resonant frequency.

Furthermore, an expression for the variation of φ_1 can be developed using Fourier series as

$$\varphi_1(t) = \left[\frac{\pi}{2} + \frac{4}{\pi} \sum_{n_1=1,3,\ldots}^{\infty} \frac{(-1)^{\frac{n_1-1}{2}}}{{n_1}^2} \sin\left\{2n_1\omega_L\left(t - \frac{T_L}{8}\right)\right\}\right] \times \left[\left(1 - \frac{4t_d}{T_L}\right) + \frac{2}{\pi} \sum_{n_2=1}^{\infty} \frac{\frac{(-1)^{n_2-1}}{n_2} \sin\left(4n_2\pi\frac{t_d}{T_L}\right)}{\times \cos\left\{2n_2\omega_L\left(t - \frac{T_L}{4}\right)\right\}}\right]. \quad (2)$$

The output voltage of the pick-up converter can also be derived as

$$V_{si} = V_{\text{out}} \frac{4}{\pi} \sum_{n=1,3\ldots}^{\infty} \frac{1}{n} \cos(n\omega_T t + n\theta) \sin\left(\frac{n\varphi_2}{2}\right). \quad (3)$$

In order to simplify the *LCCL* network shown in Fig. 2, the equivalent impedance Z_{pt} of L_p and C_p at an angular frequency ω can be defined as $Z_{pt} = L_p\omega - 1/\omega C_p$. Z_{pt} is inductive for the frequencies considered in this paper and hence, $L_{pt}\omega = Z_{pt} = L_p\omega - 1/\omega C_p$ where L_{pt} represents the equivalent inductance of L_p and C_p. Therefore, L_{pt} can be written as

$$L_{pt} = L_p - \frac{1}{\omega^2 C_p}. \quad (4)$$

Similarly on the pick-up side, L_s and C_s can be reduced by defining another equivalent inductor L_{st}, which is given by

$$L_{st} = L_s - \frac{1}{\omega^2 C_s}. \quad (5)$$

Therefore, the *LCCL* network can be reduced to an inductor–capacitor–inductor (*LCL*) network, as depicted in Fig. 6. The mutual coupling M between L_p and L_s can be expressed as $M = k\sqrt{L_p L_s}$, where k is the coefficient of coupling. Therefore, the induced voltages V_{pr} and V_{sr} of the primary and the pick-up networks can be derived as follows:

$$V_{pr} = j\omega M I_{st} \quad (6)$$

$$V_{sr} = j\omega M I_{pt}. \quad (7)$$

The currents I_{pi}, I_{si}, I_{pt}, and I_{st} for an *LCL* network are derived in [13] as given below

$$I_{pt} = \frac{1}{K}\left[\frac{I_{\text{in}} Z_p}{Z_p + j\omega L_{pt} + r_{pt}} + I_{\text{out}} \frac{j\omega M Z_s}{(Z_p + j\omega L_{pt} + r_{pt})\ (Z_s + j\omega L_{st} + r_{st})}\right] \quad (8)$$

$$I_{st} = \frac{1}{K}\left[\frac{I_{\text{out}} Z_s}{Z_s + j\omega L_{st} + r_{st}} + I_{\text{in}} \frac{j\omega M Z_p}{(Z_p + j\omega L_{pt} + r_{pt})\ (Z_s + j\omega L_{st} + r_{st})}\right] \quad (9)$$

$$I_{pi} = \frac{1}{Z_{pr} + j\omega L_{pi} + r_{pi}}\left[-I_{pr} Z_{pr} + V_{pi}\right] \quad (10)$$

$$I_{si} = \frac{1}{Z_{sr} + j\omega L_{si} + r_{si}}\left[-I_{sr} Z_{sr} + V_{si}\right] \quad (11)$$

where $I_{\text{in}} = \dfrac{V_{pi}}{r_{pi} + j\omega L_{pi}}$, $I_{\text{out}} = \dfrac{V_{si}}{r_{si} + j\omega L_{si}}$, $I_{pr} = \dfrac{j\omega M}{j\omega L_{pt} + r_{pt}} I_{st}$, $I_{sr} = \dfrac{j\omega M}{j\omega L_{st} + r_{st}} I_{pt}$,

$$Z_p = \frac{j\omega L_{pi} + r_{pi}}{1 - \omega^2 L_{pi} C_{pt} + j\omega C_{pt} r_{pi}},$$

$$Z_s = \frac{j\omega L_{si} + r_{si}}{1 - \omega^2 L_{si} C_{st} + j\omega C_{st} r_{si}},$$

$$Z_{pr} = \frac{j\omega L_{pt} + r_{pt}}{1 - \omega^2 L_{pt} C_{pt} + j\omega C_{pt} r_{pt}},$$

$$\mathrm{Z_{sr}} = \frac{\mathrm{j\omega\ L_{st} + r_{st}}}{1 - \omega^2 \mathrm{L_{st} C_{st}} + \mathrm{j\omega\ C_{st} r_{st}}}$$

and $K = 1 + \dfrac{\omega^2 M^2}{(Z_p + j\omega L_{pt} + r_{pt})\ (Z_s + j\omega L_{st} + r_{st})}$

.

Furthermore, the current I_{dc} which flows from the grid converter to the IPT primary converter can be deducted from I_{pi}, based on the operation of the switching devices of the IPT primary converter as

$$I_{\text{dc}} = \begin{cases} I_{pi}, \text{ if } S_{p5} \text{ and } S_{p8} \text{ ON} \\ -I_{pi}, \text{ if } S_{p6} \text{ and } S_{p7} \text{ ON} \\ 0, \text{ if } S_{p5} \text{ and } S_{p7} \text{ OR } S_{p6} \text{ and } S_{p8} \text{ ON}. \end{cases}$$

Thus, I_{dc} can be written as a product of I_{pi} and a function $f_{\text{primary}}(t)$ that represents the operation of the IPT primary

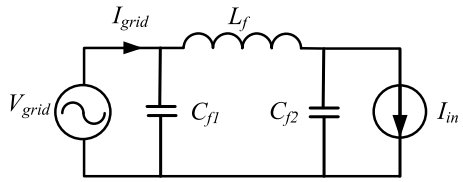

Fig. 7. Current source model of the proposed system with the input filter.

converter. According to Fig. 4, $f_{\text{primary}}(t)$ is a function that follows the exact shape of V_{pi}, however, with a unity magnitude. Therefore

$$f_{\text{primary}}(t) = \frac{4}{\pi}\sum_{n=1,3,5\ldots}^{\infty}\frac{1}{n}\cos(n\omega_T t)\sin\left(\frac{n\varphi_1}{2}\right). \quad (12)$$

Hence, I_{dc} is given by

$$\begin{aligned} I_{\text{dc}} &= I_{pi}\times f_{\text{primary}}(t) \\ &= I_{pi}\tfrac{4}{\pi}\sum_{n=1,3,5\ldots}^{\infty}\tfrac{1}{n}\cos(n\omega_T t)\sin\left(\tfrac{n\varphi_1}{2}\right). \end{aligned} \quad (13)$$

Similarly, the current I_{in} drawn by the grid converter can be expressed as

$$I_{\text{in}} = \begin{cases} I_{\text{dc}},\ \text{if } S_{p1} \text{ and } S_{p4} \text{ ON} \\ (\text{during positive half cycle of } V_{\text{grid}}) \\ -I_{\text{dc}},\ \text{if } S_{p2} \text{ and } S_{p3} \text{ ON} \\ (\text{during negative half cycle of } V_{\text{grid}}) \\ 0,\ \text{if } S_{p1}-S_{p4} \text{ OFF} \\ (\text{during deadband}). \end{cases}$$

Let $I_{\text{in}+}$ be the current drawn by the grid converter when S_{p1} and S_{p2} are turned ON. Therefore

$$I_{\text{in}+} = I_{\text{dc}} = I_{pi}\frac{4}{\pi}\sum_{n=1,3,5\ldots}^{\infty}\frac{1}{n}\cos(n\omega_T t)\sin\left(\frac{n\varphi_1}{2}\right). \quad (14)$$

From (10), (14) and substitution of expressions for I_{pr} and Z_{pr}

$$\begin{aligned} I_{\text{in}+} = &\left[\frac{1-\omega^2 L_{pt}C_{pt}+j\omega C_{pt}r_{pt}}{j\omega L_{pt}+r_{pt}+(j\omega L_{pi}+r_{pi})(1-\omega^2 L_{pt}C_{pt}+j\omega C_{pt}r_{pt})}\right] \\ &\times\left[\frac{-j\omega M I_{st}(j\omega L_{pt}+r_{pt})}{(j\omega L_{pt}+r_{pt})(1-\omega^2 L_{pt}C_{pt}+j\omega C_{pt}r_{pt})}+V_{pi}\right] \\ &\times\left[\frac{4}{\pi}\sum_{n=1,3,5\ldots}^{\infty}\frac{1}{n}\cos(n\omega_T t)\sin\left(\frac{n\phi_1}{2}\right).\right] \end{aligned} \quad (15)$$

From (15) and by analyzing the capacitor–inductor–capacitor (*CLC*) network of the low-pass filter, an analytical expression for the grid currents, drawn by the system during the positive half cycle of the grid voltage, can be derived. However, it is a tedious procedure due to the complexity of (15), which can be simplified assuming that resistances r_{pi}, r_{si}, r_{pt}, and r_{st} of primary and pick-up *LCL* network are negligibly small. Furthermore, both the primary and the pick-up *LCL* networks are tuned to the resonant frequency f_T, and hence

$$\omega_T{}^2 = (2\pi f_T)^2 = \frac{1}{L_{pi}C_{pt}} = \frac{1}{L_{pt}C_{pt}} = \frac{1}{L_{si}C_{st}} = \frac{1}{L_{st}C_{st}}. \quad (16)$$

Therefore, (15) can be simplified as

$$I_{\text{in}+} = -\frac{4}{\pi}\frac{M}{L_{pt}}I_{st}\sum_{n=1,3,5\ldots}^{\infty}\frac{1}{n}\cos(n\omega_T t)\sin\left(\frac{n\varphi_1}{2}\right). \quad (17)$$

Similarly, (9) can also be simplified to

$$I_{st} = -\frac{j}{\omega L_{si}}V_{si}. \quad (18)$$

Substituting (18) and (3) in (17) results in

$$\begin{aligned} I_{\text{in}+} = &\ \frac{16}{\pi^2}\frac{jM}{\omega L_{pt}L_{si}}V_{\text{out}} \\ &\times\left[\sum_{n_1=1,3\ldots}^{\infty}\frac{1}{n_1}\cos(n_1\omega_T t+n_1\theta)\sin\left(\frac{n_1\varphi_2}{2}\right)\right] \\ &\times\left[\sum_{n_2=1,3\ldots}^{\infty}\frac{1}{n_2}\cos(n_2\omega_T t)\sin\left(\frac{n_2\varphi_1}{2}\right)\right]. \end{aligned} \quad (19)$$

Nevertheless, due to the low-pass filter, higher order frequency components of $I_{\text{in}+}$ will be filtered out from the grid current I_{grid}. Therefore, only the fundamental frequency component of $I_{\text{in}+}$ will be considered henceforth. Consequently, (19) can be reduced to

$$\begin{aligned} I_{\text{in}+} = &\ \frac{8}{\pi^2}\frac{M}{\omega_T L_{pt,1}L_{si}}\sin\left(\frac{\varphi_1}{2}\right)\sin\left(\frac{\varphi_2}{2}\right)V_{\text{out}} \\ &\times\left[\cos\left(\theta+\frac{\pi}{2}\right)+\cos\left(2\omega_T t+\theta+\frac{\pi}{2}\right)\right] \end{aligned} \quad (20)$$

where $L_{pt,1} = L_p - \frac{1}{\omega_T{}^2 C_p}$.

From (20), it can be observed that $I_{\text{in}+}$ only depends on V_{out}, out of the input parameters of the system. As V_{out} is a constant dc voltage, $I_{\text{in}+}$ can be treated as a current source. If the current drawn by grid converter during the negative grid cycle is $I_{\text{in}-}$, then $I_{\text{in}-} = -I_{\text{in}+}$. Hence, I_{in} can be written as

$$I_{\text{in}} = I_{\text{in}+}\times f_{\text{grid}}(t) \quad (21)$$

where

$$f_{\text{grid}}(t) = \begin{cases} 1, & \text{if } V_{\text{grid}} > 0 \\ -1, & \text{if } V_{\text{grid}} < 0 \end{cases} = \tfrac{4}{\pi}\sum_{n=1,3\ldots}^{\infty}\tfrac{1}{n}\sin(n\omega_L t).$$

From (20) and (21)

$$\begin{aligned} I_{\text{in}} = &\ \frac{8}{\pi^2}\frac{M}{\omega_T L_{pt,1}L_{si}}\sin\left(\frac{\varphi_1}{2}\right)\sin\left(\frac{\varphi_2}{2}\right)V_{\text{out}} \\ &\times\left[\cos\left(\theta+\frac{\pi}{2}\right)+\cos\left(2\omega_T t+\theta+\frac{\pi}{2}\right)\right] \\ &\times\left[\frac{4}{\pi}\sum_{n=1,3\ldots}^{\infty}\frac{1}{n}\sin(n\omega_L t)\right]. \end{aligned} \quad (22)$$

As I_{in} is a current source, the entire system can be reduced to Fig. 7. From Fig. 7and by analyzing the dc component and the

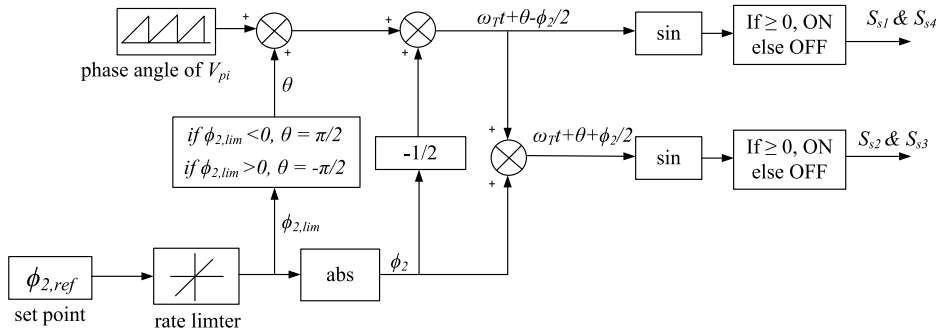

Fig. 8. Block diagram of the IPT pick-up controller.

ac component of $I_{\rm in}$ separately, the current $I_{\rm grid}$ drawn from the grid can be deducted as

$$I_{\rm grid} = jV_{\rm grid}\omega_L\left(\frac{C_{f2}}{1-{\omega_L}^2 L_f C_{f2}}+C_{f1}\right) + \left\{\left[\psi\cos\left(\theta+\tfrac{\pi}{2}\right)+\frac{\psi\cos\left(2\omega_T t+\theta+\frac{\pi}{2}\right)}{1-{\omega_T}^2 L_f C_{f2}}\right] \times\left[\frac{4}{\pi}\sum_{n=1,3\ldots}^{\infty}\frac{1}{n}\sin\left(n\omega_L t\right)\right]\right\} \tag{23}$$

where $\psi = \dfrac{8}{\pi^2}\dfrac{M}{\omega_T L_{pt,1} L_{si}} V_{\rm out}\sin\left(\dfrac{\varphi_1}{2}\right)\sin\left(\dfrac{\varphi_2}{2}\right)$.

Moreover, it can be realized that only the dc component of $I_{\rm grid}$ contributes to active power flow. Therefore, the active power $P_{\rm in}$ drawn by the system over a half cycle at grid frequency can be written as

$$P_{\rm in} = \frac{2}{T_L}\int_0^{\frac{T_L}{2}} V_{\rm grid}\psi_{\rm avg}\cos\left(\theta+\frac{\pi}{2}\right)dt = \frac{2}{T_L}\int_0^{\frac{T_L}{2}} V_{\rm in}\sin\left(\omega_L t\right)\psi_{\rm avg}\cos\left(\theta+\frac{\pi}{2}\right)dt \tag{24}$$

where $\psi_{\rm avg} = \dfrac{8}{\pi^2}\dfrac{M}{\omega_T L_{pt,1} L_{si}} V_{\rm out}\sin\left(\dfrac{\varphi_{1,\rm avg}}{2}\right)\sin\left(\dfrac{\varphi_2}{2}\right)$ and $\varphi_{1,\rm avg}$ is the average of the primary phase modulation over $T_L/2$ given by $\varphi_{1,\rm avg} = \frac{2}{T_L}\left(\dfrac{4\pi}{T_L}t_d+\pi\right)\left(\dfrac{T_L}{4}-t_d\right)$.

Therefore, (21) can be simplified to

$$P_{\rm in} = \frac{-2\psi_{\rm avg} V_{\rm in}\sin\theta}{\pi}. \tag{25}$$

From (25), it can be learnt that the power flows from the grid to the pick-up for negative values of θ whereas EV supplies power to the grid for positive θ values.

IV. Control System

An open loop control system is introduced to the pick-up side to control the magnitude and direction of the power flow of the proposed system. The block diagram of the pick-up controller is presented in Fig. 8. Based on the amount of power required, the corresponding pick-up phase modulation φ_2 can be calculated using (25) for $\theta = \pm\pi/2$, and set as the reference pick-up phase modulation $\varphi_{2,\rm ref}$ for the pick-up controller. For power flow from the primary to the pick-up, $\varphi_{2,\rm ref}$ should be positive, while for power flow from the pick-up to the primary, $\varphi_{2,\rm ref}$ should be set as a negative value. Therefore, $\varphi_{2,\rm ref}$ varies between 0 and π radians for power flow from the primary to the pick-up with $\theta = -\pi/2$, whereas it is confined between 0 and $-\pi$ radians when the power flow is from the pick-up to the primary. To ensure a smooth transfer of the set point from one value to another, $\varphi_{2,\rm ref}$ is passed through a rate limiter with a predefined value. The absolute value of the rate limited $\varphi_{2,\rm ref}$ occurs to be the pick-up phase modulation for the IPT pick-up converter, as seen from Fig. 8. Furthermore, the phase angle of the primary converter output voltage V_{pi} is employed as an input to the pick-up controller to accurately maintain the required phase shift θ of the pick-up output voltage. The resulting pick-up phase modulation φ_2 is then divided into $-\varphi_2/2$ and $\varphi_2/2$ on the time axis, and each pair of switches are operated as expounded in Fig. 8.

V. Results

A. Implementation and Converter Operation

In order to validate the proposed scheme as well as the mathematical model, a 1.1-kW BTBC-based BD-IPT system was designed and simulated in MATLAB. Moreover, a prototype, which is shown in Fig. 9, was built and tested under laboratory conditions. The grid converter, constructed with a Microsemi APTGF30H60T1G full-bridge IGBT module, was connected to the utility grid with a small low-pass filter at the front end. The output of the grid converter was connected to the IPT primary converter. An unpolarized small capacitor of 33 nF was employed in the dc-link to suppress high-frequency differential mode noise. For primary and pick-up windings, DD IPT pads were used with an air gap of 150 mm between them. The input of the IPT pick-up converter was connected to an active dc load with a 200-V power supply across it. Both the IPT primary and the pick-up converters were constructed with Fairchild Semiconductor HGTG12N60A4D IGBTs, and they were operated at a switching frequency of 20 kHz, which was the same as

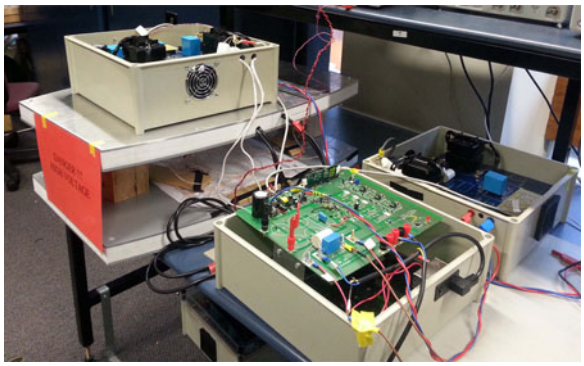

Fig. 9. Experimental setup of grid integrated BTBC-based BD-IPT system.

TABLE I
PARAMETERS OF THE PROTOTYPE BD-IPT SYSTEM

Parameter	Value
$V_{\rm in}$ (Peak Grid Voltage)	325 V
$V_{\rm out}$	200 V
L_{pi} and L_{si}	99 μH
L_p and L_s	155 μH
C_{pt} and C_{st}	0.66 μF
C_p and C_s	1.16 μF
r_{pi} and r_{si}	12 mΩ
r_{pt} and r_{st}	30 mΩ
L_f	80 μH
C_{f1}	3.3 μF
C_{f2}	4.92 μF
k	0.32
Air gap	150 mm
f_T	20 kHz
Grid frequency	50 Hz

the resonant frequency of the *LCCL* network. A complete list of circuit parameters of the prototype system are provided in Table I. The switching algorithms for the grid converter, the IPT primary and the pick-up converter were implemented on a Texas Instruments TMS320F28335 Digital Signal Controller (DSC). A software phase-locked loop (PLL), which can synchronize with the grid voltage, was also implemented on the DSC. Based on the phase output of the PLL, switching signals to drive the converters are produced by the DSC.

The gate driver voltages and switch voltages across S_{p1} and S_{p2} of the grid converter are depicted in Fig. 10 together with the voltage of the soft dc-link to demonstrate near zero-voltage switching of the grid converter experimentally. As the waveforms of S_{p3} and S_{p4} are similar to those of S_{p1} and S_{p2}, respectively, with a phase shift of 180°, they are not provided here. As evident from Fig. 10, from $t = 0$ to $t = 1$ ms, the voltage of the utility grid is close to zero. Thus, the grid converter remains at its deadband operation by turning OFF all its switches. It can be seen from Fig. 10 that the voltage across S_{p2} also remains nearly at zero during the deadband. At $t = 1$ ms, after the deadband period is elapsed, a gate voltage of 13 V is applied to S_{p2} to turn it ON. Hence, near zero-voltage switching occurs with S_{p2} at $t = 1$ ms. S_{p3} is also turned ON at the same time, and therefore, a voltage that is equal to the grid voltage but opposite

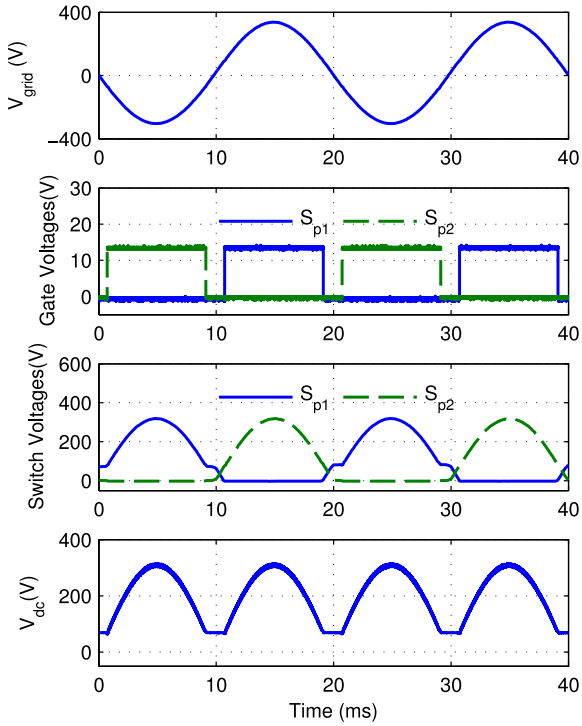

Fig. 10. Gate voltages, switch voltages of grid converter and soft dc-link voltage (experimental).

in sign is resulted across the dc-link $V_{\rm dc}$. Moreover, as S_{p2} turns ON, the voltage across the dc-link is applied across S_{p1} during this time frame, as shown in the Fig. 10. At $t = 9$ ms, the converter enters the deadband again, where S_{p2} and S_{p3} are made to turn OFF by applying a zero voltage to the respective IGBT gate terminals. Consequently, the voltage across S_{p2} should ideally start increasing. However, IGBTs essentially have a capacitance between the collector and emitter terminals. Therefore, S_{p2} retains its previous voltage after it is turned OFF, as there is no discharge path for its collector–emitter capacitance during the deadband. Hence, the voltage across S_{p1} also remains constant at $V_{\rm dc}$ until the polarity of the grid voltage reverses at $t = 10$ ms. Moreover, since the IPT primary converter is essentially disconnected from the dc-link during the deadband, the small capacitor at the dc-link retains its voltage over the deadband, as evident from Fig. 10. At $t = 10$ ms, with the reversal of grid voltage, S_{p2} and S_{p3} become reverse biased, and thus, voltages across S_{p1} and S_{p2} start to gradually decrease and increase, respectively. When the grid voltage is very close to the voltage at the dc-link, S_{p1} is turned ON along with S_{p4}. As a result, near zero-voltage switching occurs with S_{p1} at $t = 11$ ms. Similarly, S_{p3} and S_{p4} are also switched only when their respective voltages are near zero. Moreover, the collector–emitter capacitance of S_{p2} and S_{p4} are found to be slightly higher than that of S_{p1} and S_{p3}. Therefore, similar to S_{p2}, S_{p4} also retains its voltage at zero after it is turned OFF and, hence, the overall shape of the voltage waveform of S_{p1} (or S_{p3}) slightly differs from that of S_{p2} (or S_{p4}).

Fig. 11 presents the experimental voltages of V_{pa}, V_{pb}, V_{pi}, and V_{si} over a period of 250 μs. As explained in Section II,

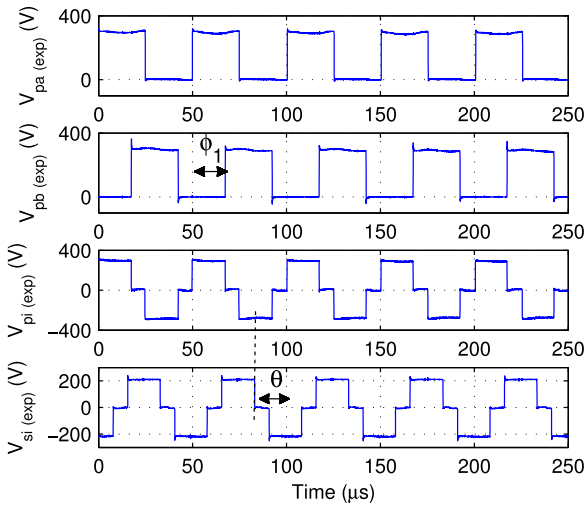

Fig. 11. V_{pa},V_{pb},V_{pi}, and V_{si} (experimental).

both V_{pa} and V_{pb} are square wave voltages with magnitudes equal to the dc-bus voltage. The phase delay between V_{pa} and V_{pb}, which is essentially the primary phase modulation φ_1 is about 15 μs, which corresponds to a phase shift of 108° at an operating frequency of 20 kHz. Due to the difference of V_{pa} and V_{pb}, the output voltage V_{pi} of the primary IPT converter, which drives the *LCCL* resonant network, is manifested as shown in the Fig. 11. Similarly, V_{si} that holds the same frequency as V_{pi} is produced by the IPT pick-up converter on the pick-up side. According to the Fig. 11, the relative phase angle θ is about $-90°$ for transferring power from the primary to the pick-up.

In order to demonstrate the validity of the proposed system and the mathematical analysis, the system was tested under three test cases as shown below:

1) *forward, full power operation:* system delivers its maximum power from the utility grid to the active load;
2) *forward, half power operation:* system regulates the power flow to half of the maximum power and delivers it from the utility grid to the active load;
3) *reverse, full power operation:* system delivers its maximum power from the pick-up to the utility grid.

B. Forward, Full Power Operation

Theoretical, simulated, and experimental results showing steady-state output voltage V_{pi} of the BTBC, output current I_{pi} of the BTBC, output voltage V_{si}, and output current I_{si} of the IPT pick-up converter over a 150 μs period are illustrated in Fig. 12. Theoretical waveforms were obtained using the proposed mathematical analyses up to the 50$^{\text{th}}$ harmonic. Although, V_{pi} in Fig. 12(a)–(c) vary with the utility grid voltage according to (1), results were captured when the grid voltage was at its maximum of 325 V. Hence, the primary phase modulation φ_1 is also at its maximum of π radians, as evident from Fig. 12. For the forward power operation, the IPT pick-up converter is operated with a relative phase angle θ at $-\pi/2$ according to (25), and as a result, V_{pi} leads V_{si} by 90°. Furthermore, in order to have maximum or full power operation, pick-up phase modulation is maintained at π radians. The output current I_{pi} of the BTBC is in phase with the output voltage V_{pi}, and this leads to unity power factor operation of the primary. V_{si} and I_{si} are displaced by 180° and, hence, the pick-up system also operates at unity power factor, but with current flowing in the reverse direction into the active load.

Fig. 13 depicts the grid current of the system, obtained using the mathematical model, simulation model, and the experimental prototype over a period of 40 ms. As expected from (23), the grid current remains close to zero during the deadband, and closely follows a shape of a sinusoidal waveform during normal operation. Furthermore, it is in phase with the utility grid voltage, making power factor of the overall system close to unity. As observed from Fig. 13(c), I_{grid} gathered from the experimental prototype is around 5.3 A, which is slightly higher than that of obtained from both the mathematical model and the simulation model. Hence, the experimental system draws an average power of approximately 1.2 kW from the utility grid, while both theoretical and simulation models draw only about 1.1 kW. This discrepancy could be attributed to resistances of inductors and semiconductor losses of converters. Nevertheless, theoretical, simulated, and experimental results, shown in both Figs. 12 and 13, appear to be in good agreement with each other. As a result, the validity of the proposed mathematical model is verified for forward, full power operation.

C. Forward, Half Power Operation

In order to demonstrate system's capability to regulate the amount of power transfer, the pick-up phase modulation φ_2 has been decreased to $\pi/3$, while maintaining the relative phase angle θ at $-\pi/2$ for forward power flow. The resulting theoretical, simulated, and experimental waveforms for V_{pi}, I_{pi}, V_{si}, and I_{si} are portrayed in Fig. 14, and grid current I_{grid} along with grid voltage V_{grid} are depicted in Fig. 15. The duty cycle of V_{si} has dropped to 33% as predicted by (3), due to the reduction of φ_2 to $\pi/3$. According to (23), the grid current has a small reactive current component mainly drawn by the low-pass filter, and it does not depend on φ_2. Thus, the grid current drawn by the system in half power mode is slightly higher than 50% of the grid current drawn by the system at full power mode, as evident from Fig. 15(a)–(c). Nevertheless, the average power drawn by the system is dropped by half of system's full power rating, according to (25). Therefore, this verifies the capability of the proposed system to regulate the magnitude of power flow by controlling the pick-up phase modulation φ_2.

D. Reverse, Full Power Operation

Theoretical and simulated results are plotted along with experimental results in Figs. 16 and 17, when the proposed system is operated with a θ of $\pi/2$ and φ_2 of π radians, in order to supply the maximum power to the primary or the utility grid from the pick up. In comparison to Fig. 12, V_{pi} and I_{pi} in Fig. 16 are out of phase by 180°, whereas, V_{si} and I_{si} are in phase. The direction of grid current in Fig. 17 is reversed in contrast to Fig. 13, although the magnitude remains approximately the

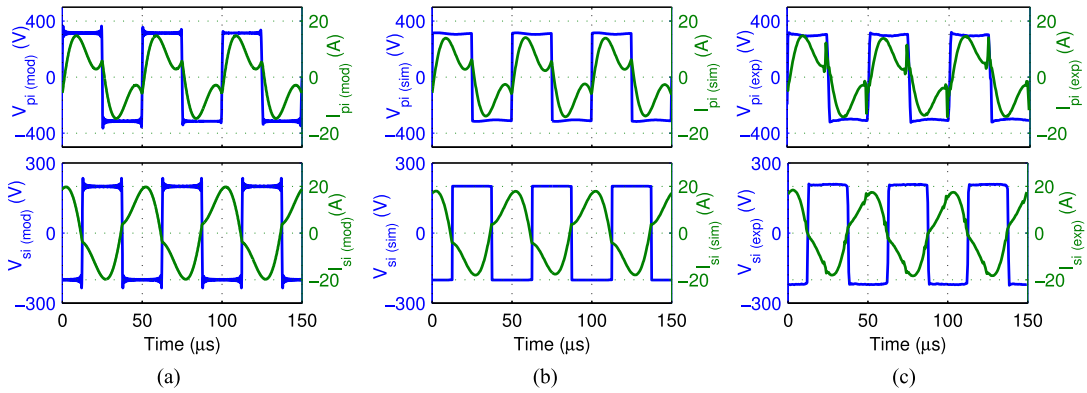

Fig. 12. Waveforms of IPT primary and pick-up converters at $\varphi_2 = \pi$ and $\theta = -\pi/2$ (a) theoretical (b) simulated and (c) experimental.

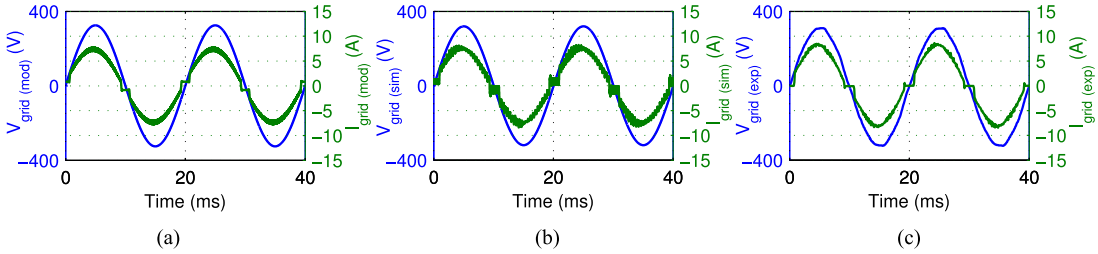

Fig. 13. Waveforms on the grid side at $\varphi_2 = \pi$ and $\theta = -\pi/2$ (a) theoretical (b) simulated and (c) experimental.

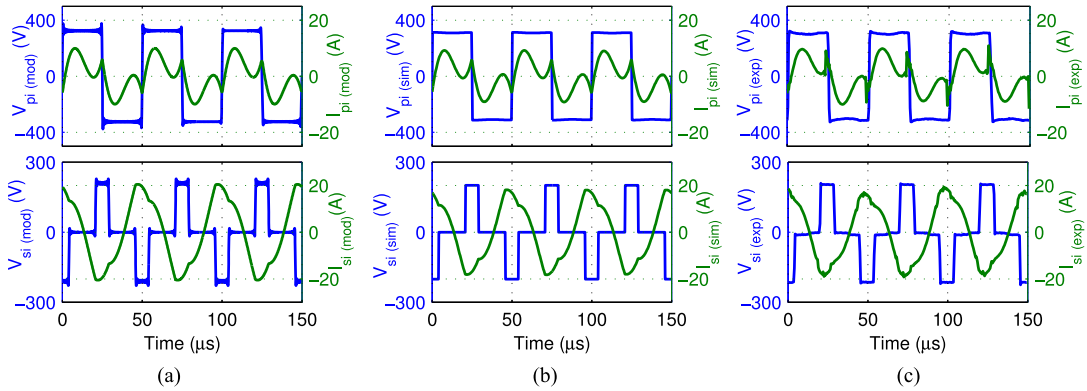

Fig. 14. Waveforms of IPT primary and pick-up converters at $\varphi_2 = \pi/3$ and $\theta = -\pi/2$ (a) theoretical (b) simulated and (c) experimental.

same, as expected from (23). Thus, the system delivers about 1 kW on average to the utility grid, adhering to (25). Consistency of theoretical, simulation, and experimental results presented in both Figs. 16 and 17 verifies the accuracy of the mathematical model for reverse power flow as well.

E. Dynamic Performance

The performance of the proposed system under transient conditions was also tested and the experimental results are presented in Figs. 18 and 19. Fig. 18(a) portrays a situation, where the magnitude of the power flow is reduced by decreasing the pick-up phase modulation φ_2. Over the first 500 ms, the system draws about 1.1 kW from the utility grid at a φ_2 of π and θ of $-\pi/2$ radians, for forward power flow. At $t = 500$ ms, the reference pick-up phase modulation $\varphi_{2,\mathrm{ref}}$ in Fig. 8 is set to $\pi/3$ to reduce the amount of power transfer, and hence, φ_2 starts to decrease at a predefined rate of $4\pi/3$ rad/s until it reaches the value of the new set point at $t = 1000$ ms. The new set point of $\varphi_{2,\mathrm{ref}} = \pi/3$ corresponds to previously discussed forward, half power operation of the system, and therefore, it draws only about 650 W from the utility grid as expected.

The experimental results obtained from the prototype, when the direction of the power flow was reversed are depicted in Fig. 18(b). From $t = 0$ to $t = 500$ ms, $\varphi_{2,\mathrm{ref}}$ and θ are set to $-2\pi/3$ and $\pi/2$, respectively, for reverse power flow. Thus, the system supplies about 950 W from the pick-up to the utility grid which is depicted as a negative power in Fig. 18(b). At $t = 500$

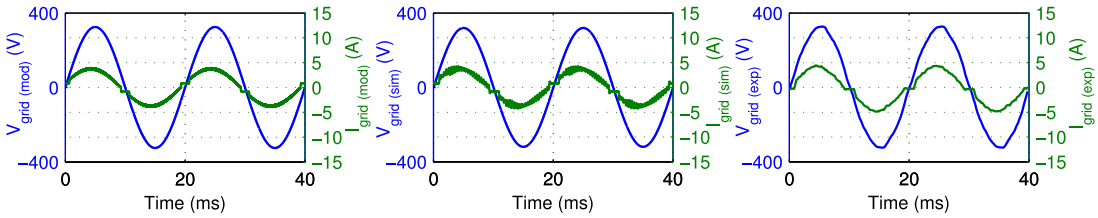

Fig. 15. Waveforms on the grid side at $\varphi_2 = \pi/3$ and $\theta = -\pi/2$ (a) theoretical (b) simulated and (c) experimental.

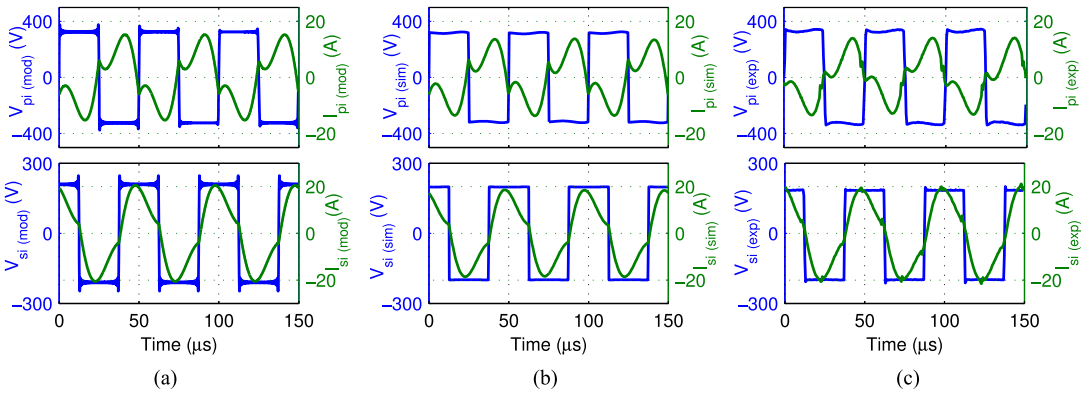

Fig. 16. Waveforms of IPT primary and pick-up converters at $\varphi_2 = \pi$ and $\theta = \pi/2$ (a) theoretical (b) simulated and (c) experimental.

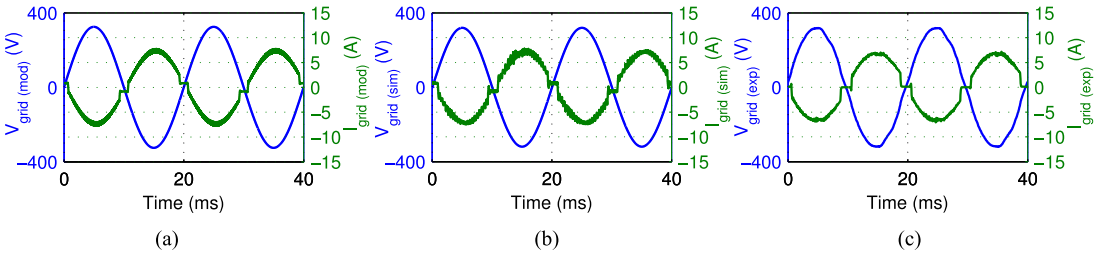

Fig. 17. Waveforms on the grid side at $\varphi_2 = \pi$ and $\theta = \pi/2$ (a) theoretical (b) simulated and (c) experimental.

ms, $\varphi_{2,\mathrm{ref}}$ is given a new set point of $2\pi/3$ for forward power flow. As a result, the pick-up phase modulation φ_2 slides down to zero at a rate of $4\pi/3$ rad/s until it reaches zero at 1000 ms. As φ_2 reduces, the power supplied by the pick-up also reduces proportionally. When φ_2 reaches zero, the power drawn by the system from the pick-up becomes very small, which is too low to supply the losses incurred by the primary side of the system. Hence, the primary side starts to draw power from the grid just before 1000 ms, where θ is set to $-\pi/2$ for forward power flow. Consequently, φ_2 starts to increase again at the same rate until it reaches its final value of $2\pi/3$ radians at $t = 1500$ ms. The power drawn by the system should ideally be about 950 W, but it draws slightly over 1 kW due to losses of the system.

Fig. 19 illustrates a magnified view of the grid currents along with the grid voltage for a situation, where the power flow is reversed. Initially, the grid current is out of phase with the grid voltage by 180° and, hence, the pick-up is supplying power to the grid. The phase angle between the grid current and the grid voltage gradually decreases with time and becomes almost zero around $t = 400$ ms in order to supply the power from the grid to the pick up. Moreover, the magnitude of the grid current also reduces as φ_2 reduces until θ is reversed around 200 ms. However, due to the losses and the input filter, the magnitude of the current does not reach zero.

F. Total Harmonic Distortion and Power Factor

Using the prototype, harmonic magnitudes of the grid current I_{grid} as a percentage of fundamental are calculated, and plotted in Fig. 20 up to the 20$^{\mathrm{th}}$ harmonic, when the system is delivering power to the active load at a φ_2 of π. As evident from Fig. 20, the third and seventh harmonic of the grid current is about 7% and 4% of the fundamental, respectively, whereas, all the other harmonics have a magnitude below 4% of the fundamental. According to Australian Standards (AS 4777.2-2005) the limit for third, fifth, seventh, and ninth harmonic of the grid current

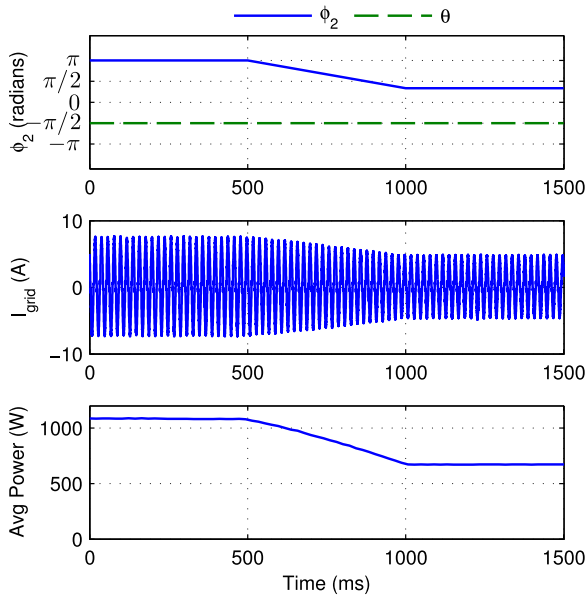

(a)

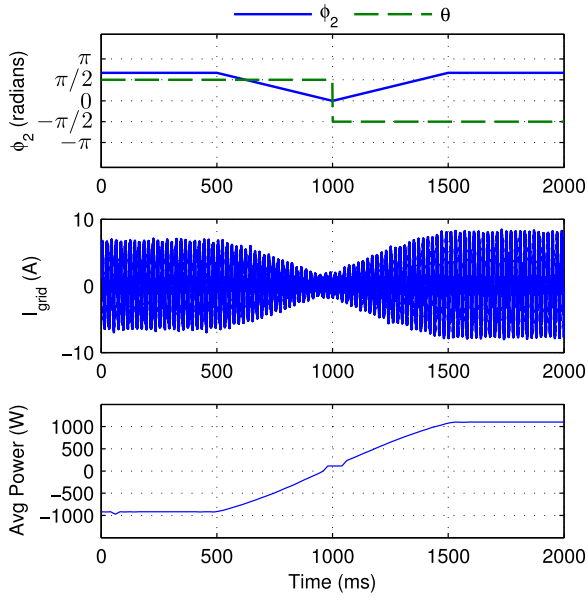

(b)

Fig. 18. Pick-up phase modulation, relative phase angle, grid current, and average power (experimental) (a) change of magnitude of power flow (b) change of direction of power flow.

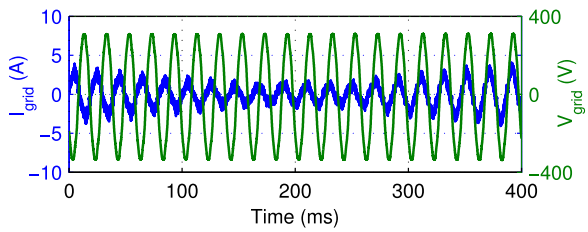

Fig. 19. Grid current and grid voltage when the direction of power flow is reversed (experimental).

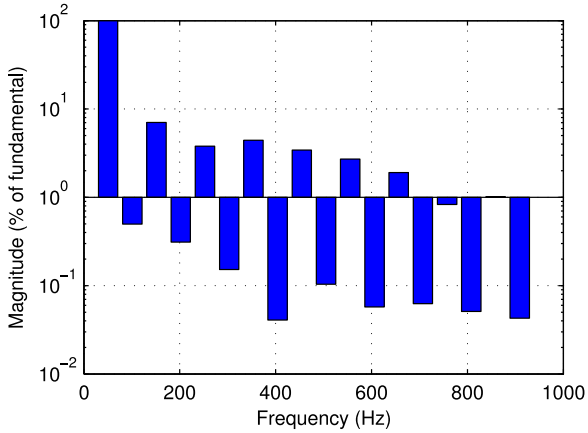

Fig. 20. Magnitudes of harmonics of $I_{\rm grid}$ at $\varphi_2 = \pi$ and $\theta = -\pi/2$ (experimental).

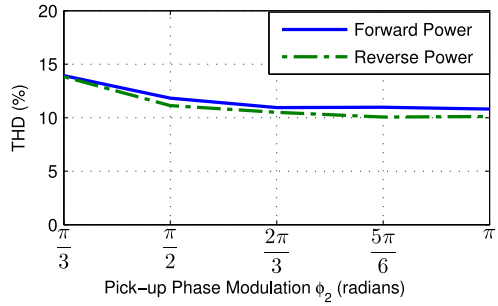

Fig. 21. THD of the grid current up to the 50th harmonic (experimental).

is defined as 4% of the fundamental. Therefore, third harmonic content of the grid current slightly exceeds the limit set by the standards. However, third harmonic content of the grid current can be reduced by optimizing the modulation strategy and also by minimizing the deadband, which contributes to distortion of the shape of the grid current near zero.

Fig. 21 illustrates the THD of the grid current of the experimental prototype up to the 50th harmonic against φ_2, for both forward and reverse power operations. As the amount of power transferred is relatively low, φ_2 values below are not considered. As observed from Fig. 21, the grid current THD for both forward and reverse power operation decreases with φ_2. As the current $I_{\rm in}$ drawn by the grid converter decreases as φ_2 decreases, according to (22), the reactive current that is independent of φ_2 becomes more apparent for lower values of φ_2. Therefore $I_{\rm grid}$, which consists of $I_{\rm in}$ and reactive currents drawn by the low-pass filter, gets more distorted as φ_2 decreases. Thus, the grid current THD displays relatively higher values for lower φ_2. Moreover, in a practical system, the values of tuning capacitors and inductors are subjected to change slightly, due to factors such as component tolerances and temperature variations. Therefore, the resonant networks get detuned by a very small scale. In such a scenario, the input impedance of the system seen by the IPT primary converter is slightly inductive or capacitive, and depends on relative phase angle θ, as described in [13]. Hence, the grid current essentially has a very small, but

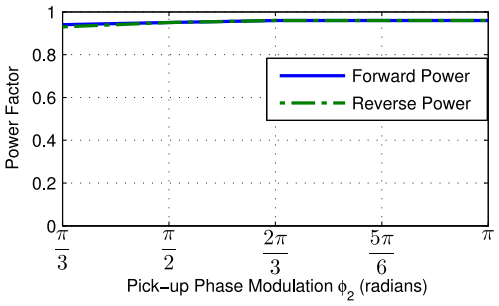

Fig. 22. Power factor of the overall system (experimental).

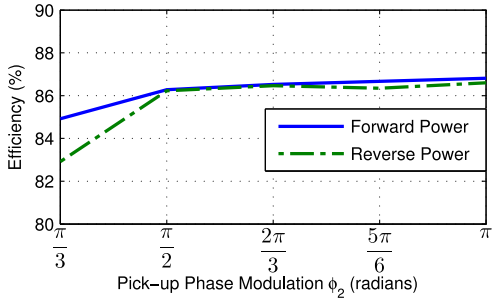

Fig. 23. Overall efficiency of the system (experimental).

different reactive current components for forward and reverse power operation. As a result, the values obtained for grid current THD in Fig. 21 for forward and reverse power flow deviate from each other by a very narrow margin, though they are expected to be the same for an ideal system.

The overall power factor of the system, experimentally measured from the grid side, is presented against φ_2 in Fig. 22 for both forward and reverse power flow. As previously mentioned, though the magnitude of the active power drawn or supplied by the system decreases with a reduction in φ_2, the magnitude of the reactive power drawn by the system, remains the same. This leads to a slight dip in the system power factor below 0.96 for lower φ_2 values, especially for φ_2 below $2\pi/3$ radians, as observed in Fig. 22. Nonetheless, for either direction of power flow, the system generally displays a power factor very close to unity, throughout the range of φ_2 considered here.

G. Efficiency, Losses, and Reliability

The overall efficiency of the system from the utility grid to the output of the IPT pick-up converter was calculated and illustrated in Fig. 23 for both directions of power flow. The average voltage across the soft dc-link of the proposed system is lower than that of a conventional system with a stiff dc-link, as the soft dc-link of the proposed system operates with a large voltage ripple. Therefore, the IPT primary converter of the proposed system draws a higher average current to transfer the same amount of power as in a conventional system. This results in comparatively higher semiconductor losses in the IPT primary converter as well as higher copper losses in the series inductor L_{pi} and in connecting cables. Hence, a slight reduction in the overall efficiency is expected with the proposed system. Nevertheless, the system displays a consistent efficiency that approximately equals to 87%, when φ_2 is above $\pi/2$ radians for forward as well as reverse direction of power flow.

TABLE II
THERMAL RESISTANCES OF CONVERTERS

Converter	Thermal Resistance (°C/W)
Grid Converter	0.7
IPT Primary Converter	1.2
IPT Pick-up Converter	0.9

It is important to gain an insight into the losses of the system, to explain the efficiency of the proposed system. Although, both semiconductor and copper losses of the BTBC-based BD-IPT system can be expressed analytically, it is a tedious procedure due to the complexity of the current expressions given in Section III. Furthermore, measuring the losses accurately using the prototype is also a difficult task due to inaccessibility of some of the required measurement points in the circuit layout. However, the semiconductor loss $P_{\rm loss}$ of a converter is generally related to the temperature rise of its heat sinks as

$$P_{\rm loss} = \frac{T_H - T_A}{R_{th}} \tag{26}$$

where T_H, T_H, and R_{th} denote the steady-state temperature of the heat sink, ambient temperature, and the thermal resistance of the heat sink, respectively.

In order to measure the thermal resistance of the heat sinks of the grid converter, both the inputs and outputs of the converter were disconnected, and then the input was supplied with a current limited dc source while maintaining $S_{p1} - S_{p4}$ at ON state. By measuring the steady-state temperature of the heat sink, ambient temperature and the power drawn by the grid converter, the thermal resistance $R_{th,\rm grid}$ of the heat sink of the grid converter were calculated using (26). Similarly, the thermal resistances $R_{th,\rm prim}$ and $R_{th,\rm pick}$ of the heat sinks of the IPT primary converter and the IPT pick-up converter were calculated, respectively, and shown in Table II. Hence, by measuring the steady-state temperatures of the heat sinks of each converter, semiconductor losses of each converter can be estimated using (26). Furthermore, copper losses P_{cu} of the system can also be given by

$$P_{cu} = P_{\rm in} - (P_{\rm out} + P_{\rm grid} + P_{\rm prim} + P_{\rm pick-up}) \tag{27}$$

where $P_{\rm in}$ = power input of the system, $P_{\rm out}$ = power output of the system, $P_{\rm grid}$ = semiconductor loss in the grid converter, $P_{\rm prim}$ = semiconductor loss in the IPT primary converter, and $P_{\rm pick-up}$ = semiconductor loss in the IPT pick-up converter.

As observed in Fig. 23, the difference between the efficiency for the forward power operation and that for the reverse power operation is less than 1% for the majority of the focused operational range. Therefore, both the semiconductor and the copper losses incurred by the system for forward and reverse power operations can be assumed approximately the same. Hence, the losses were calculated only for forward power operation of the

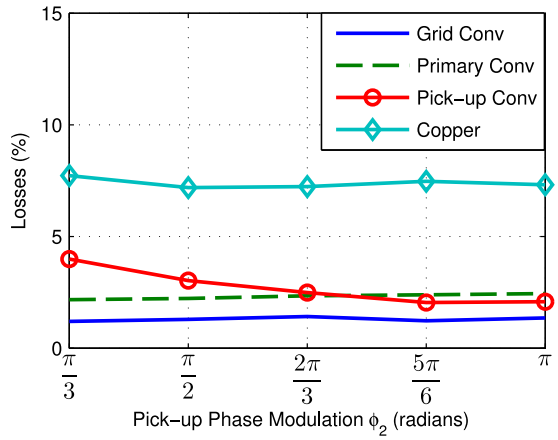

Fig. 24. Estimated semiconductor losses and copper losses.

system. Variation of the estimated semiconductor loss of each converter and the total estimated copper loss of the system as a percentage of the input power against the pick-up phase modulation φ_2 are presented in Fig. 24. Out of the three converters, the grid converter accounts for the minimum losses as expected due to its lower operating frequency and near zero-voltage switching. The current I_{pi} drawn by the IPT primary converter is a function of φ_2, whereas I_{si} drawn by the IPT pick-up converter is independent φ_2 of as evident from (3) and (8)–(11). Therefore, for lower φ_2 values, I_{pi} is lower than I_{si}, and hence, the IPT primary converter generates lower losses than the IPT pick-up converter, though, both of them are operated at the same switching frequency. The semiconductor losses incurred by each converter are much lower than the copper loss of the system. The higher copper loss is caused by the resistances of connecting cables and inductors of the resonant network. By optimizing the hardware design, copper losses associated with connecting cables can be reduced and, hence, the efficiency can be made slightly higher.

Furthermore, the reliability of the semiconductors of a given converter is significantly influenced by junction temperatures of the semiconductor devices used. However, junction temperatures of the semiconductor devices are proportional to the losses incurred by them [23]–[25]. Thus, it can be understood that the semiconductor devices of the grid converter of the proposed system hold a higher reliability than those of IPT primary and pick-up converters as the grid converter incurs the least semiconductor losses over the focused operational range.

H. Discussion

In order to justify the suitability of the proposed system, it is important to make a comparison of it with existing systems. In the literature, the experimental efficiency of a grid-connected BD-IPT system that has been employed for EV charging applications is not reported yet. Nevertheless, the overall efficiency of a recently reported dc source-based BD-IPT system are discussed in [13]. The IPT primary converter as well as the pick-up converter of these systems are supplied with a constant dc voltage which is generated by a dc power supply at their respective inputs, and hence they do not require a grid converter. Nonetheless, the system stated in [13] is capable of transferring up to 1.1 kW at a maximum overall efficiency of about 90%. Furthermore, latest unidirectional IPT systems for EV charging are reported in [5] and [26]–[28]. The system described in [26] holds a maximum efficiency of 74%, while transferring 27 kW. Overall efficiencies of the two unidirectional IPT systems explained in [27] and [28] have attained a maximum efficiency of 80% at 1.5 kW and 85% at 300 W, respectively. The EV charging system described in [5], which has been designed and optimized for improving the efficiency, has achieved an overall efficiency slightly above 90% at 5 kW. In addition, its authors have claimed that the system proposed by them is the inductive level 2 (240 V ac) charging system with the highest overall efficiency. Therefore, the proposed BTBC-based BD-IPT system is more efficient than many of the recently reported inductively coupled EV charging systems, although its efficiency is slightly lower than that of the most efficient inductively coupled EV charging system reported in the literature.

A conventional system that can transfer a power around 1 kW typically employs a dc-link capacitor with a value ranging from several hundreds of microfarads to few millifarads with a voltage rating higher than the peak grid voltage. Moreover, the input inductor of such a systems is generally about several millihenrys with a current rating closer to 5 A. Therefore, elimination of the dc-link capacitor as well as the input inductor with the proposed system accounts for a considerable reduction of cost. Furthermore, a typical input inductor on the grid side is bulky and weighs up to several kilograms. Hence, the converters of the proposed system are able to achieve a significant weight reduction by the elimination of the input inductor and the dc-link capacitor. Therefore, the proposed system can outweigh its slight decline in efficiency by a reduction of system cost and weight.

VI. Conclusion

A dc-link capacitor and an input inductor-free, bidirectional, contactless grid interface, which is based on inductive power transfer (IPT), has been proposed for V2G and G2V systems. The proposed grid interface comprises two converters in back-to-back configuration, and has the ability to regulate both the magnitude and the direction of power flow. In contrast to existing systems, the grid converter can be operated at a much lower switching frequency using a simpler switching strategy. A mathematical model that can estimate grid currents, converter voltages, and currents has been proposed. In order to investigate the feasibility of the proposed scheme, as well as the accuracy of the mathematical model, a MATLAB simulation model and a 1.1-kW experimental prototype have been developed and tested, presenting results under various operating conditions. Good agreement between theoretical, simulation, and experimental results validates the accuracy of the proposed mathematical model. Moreover, the THD of the grid current, the power factor, and the efficiency of the experimental prototype have been investigated for both directions of power flow, and the results suggest that the system exhibits a steady efficiency profile

with reasonably low THD and a unity power factor, throughout the considered operational range.

REFERENCES

[1] J. Sexauer, K. McBee, and K. Bloch, "Applications of probability model to analyze the effects of electric vehicle chargers on distribution transformers," *IEEE Trans. Power Syst.*, vol. 28, no. 2, pp. 847–854, Oct. 2013.

[2] M. Etezadi-Amoli, K. Choma, and J. Stefani, "Rapid-charge electric-vehicle stations," *IEEE Trans. Power Del.*, vol. 25, no. 3, pp. 1883–1887, Jul. 2010.

[3] Z. Wang and S. Wang, "Grid power peak shaving and valley filling using vehicle-to-grid systems," *IEEE Trans. Power Del.*, vol. 28, no. 3, pp. 1822–1829, Jul. 2013.

[4] M. Yilmaz and P. Krein, "Review of the impact of vehicle-to-grid technologies on distribution systems and utility interfaces," *IEEE Trans. Power Electron.*, vol. 28, no. 12, pp. 5673–5689, Dec. 2013.

[5] H. Wu, A. Gilchrist, K. Sealy, and D. Bronson, "A high efficiency 5 kW inductive charger for EVs using dual side control," *IEEE Trans. Ind. Informat.*, vol. 8, no. 3, pp. 585–595, Aug. 2012.

[6] A. W. Green and J. T. Boys, "10 kHz inductively coupled power transfer-concept and control," in *Proc. Fifth Int. Conf. Power Electron. Variable-Speed Drives*, Oct. 1994, pp. 694–699.

[7] S. R. Hui and W. Ho, "A new generation of universal contactless battery charging platform for portable consumer electronic equipment," *IEEE Trans. Power Electron.*, vol. 20, no. 3, pp. 620–627, Jun. 2005.

[8] P. Si, A. P. Hu, S. Malpas, and D. Budgett, "A frequency control method for regulating wireless power to implantable devices," *IEEE Trans. Biomed. Circuits Syst.*, vol. 2, no. 1, pp. 22–29, Mar. 2008.

[9] U. K. Madawala and D. J. Thrimawithana, "A bidirectional inductive power interface for electric vehicles in V2G systems," *IEEE Trans. Ind. Electron.*, vol. 58, no. 10, pp. 4789–4796, Oct. 2011.

[10] J. Huh, S. Lee, C. Park, G.-H. Cho, and C.-T. Rim, "High performance inductive power transfer system with narrow rail width for on-line electric vehicles," in *Proc. IEEE Energy Convers. Congr. Expo.*, Sep. 2010, pp. 647–651.

[11] J. M. Miller, O. Onar, C. White, S. Campbell, C. Coomer, L. Seiber, R. Sepe, and A. Steyerl, "Demonstrating dynamic wireless charging of an electric vehicle: The benefit of electrochemical capacitor smoothing," *IEEE Power Electron. Mag.*, vol. 1, no. 1, pp. 12–24, Mar. 2014.

[12] T. Imura and Y. Hori, "Maximizing air gap and efficiency of magnetic resonant coupling for wireless power transfer using equivalent circuit and Neumann formula," *IEEE Trans. Ind. Electron.*, vol. 58, no. 10, pp. 4746–4752, Oct. 2011.

[13] D. J. Thrimawithana and U. K. Madawala, "A generalized steady-state model for bidirectional IPT systems," *IEEE Trans. Power Electron.*, vol. 28, no. 10, pp. 4681–4689, Oct. 2013.

[14] R. Miskiewicz, A. Moradewicz, and M. Kazmierkowski, "Contactless battery charger with bi-directional energy transfer for plug-in vehicles with vehicle-to-grid capability," in *Proc. IEEE Int. Symp. Ind. Electron.*, 2011, pp. 1969–1973.

[15] D. J. Thrimawithana and U. K. Madawala, "A novel matrix converter based bi-directional IPT power interface for V2G applications," in *Proc. Energy Conf. Exhib.*, Dec. 2010, pp. 495–500.

[16] V. A. Sankaran, F. L. Rees, and C. S. Avant, "Electrolytic capacitor life testing and prediction," in *Proc. 32nd IAS Annu. Meeting Conf. Record Ind. Appl. Conf.*, Oct. 1997, vol. 2, pp. 1058–1065.

[17] M. Vogelsberger, T. Wiesinger, and H. Ertl, "Life-cycle monitoring and voltage-managing unit for DC-link electrolytic capacitors in PWM converters," *IEEE Trans. Power Electron.*, vol. 26, no. 2, pp. 493–503, Feb. 2011.

[18] D. Segaran, D. Holmes, and B. P. McGrath, "High-performance bi-directional AC–DC converters for PHEV with minimised DC bus capacitance," in *Proc. IEEE 37th Annu. Conf. Ind. Electron. Soc.*, Nov. 2011, pp. 3620–3625.

[19] P. W. Wheeler, J. Rodriguez, J. C. Clare, L. Empringham, and A. Weinstein, "Matrix converters: A technology review," *IEEE Trans. Ind. Electron.*, vol. 49, no. 2, pp. 276–288, Apr. 2002.

[20] K. Sun, D. Zhou, L. Huang, K. Matsuse, and K. Sasagawa, "A novel commutation method of matrix converter fed induction motor drive using RB-IGBT," *IEEE Trans. Ind. Appl.*, vol. 43, no. 3, pp. 777–786, May 2007.

[21] P. Wheeler, J. Clare, L. Empringharn, M. Bland, and M. Apap, "Gate drive level intelligence and current sensing for matrix converter current commutation," *IEEE Trans. Ind. Electron.*, vol. 49, no. 2, pp. 382–389, Apr. 2002.

[22] D. S. B. Weerasinghe, U. K. Madawala, D. J. Thrimawithana, and D. M. Vilathgamuwa, "A technique for improving grid side harmonic distortion of matrix converter based bi-directional IPT systems," in *Proc. IEEE 39th Annu. Conf. Ind. Electron. Soc.*, 2013, pp. 334–339.

[23] B. Abdi, A. Ranjbar, G. Gharehpetian, and J. Milimonfared, "Reliability considerations for parallel performance of semiconductor switches in high-power switching power supplies," *IEEE Trans. Ind. Electron.*, vol. 56, no. 6, pp. 2133–2139, Jun. 2009.

[24] W. Zhou, X. Zhong, and K. Sheng, "High temperature stability and the performance degradation of SiC MOSFETs," *IEEE Trans. Power Electron.*, vol. 29, no. 5, pp. 2329–2337, May 2014.

[25] D. Hirschmann, D. Tissen, S. Schroder, and R. De Doncker, "Reliability prediction for inverters in hybrid electrical vehicles," *IEEE Trans. Power Electron.*, vol. 22, no. 6, pp. 2511–2517, Nov. 2007.

[26] J. Huh, S. Lee, W. Lee, G. Cho, and C. Rim, "Narrow-width inductive power transfer system for online electrical vehicles," *IEEE Trans. Power Electron.*, vol. 26, no. 12, pp. 3666–3679, Dec. 2011.

[27] C.-Y. Huang, J. T. Boys, and G. A. Covic, "LCL pickup circulating current controller for inductive power transfer systems," *IEEE Trans. Power Electron.*, vol. 28, no. 4, pp. 2081–2093, Apr. 2013.

[28] N. X. Bac, D. M. Vilathgamuwa, and U. K. Madawala, "A SiC-based matrix converter topology for inductive power transfer system," *IEEE Trans. Power Electron.*, vol. 29, no. 8, pp. 4029–4038, Aug. 2014.

Saranga Weerasinghe (S'12) received B.Sc. Eng. (Hons.) degree in electrical engineering from the University of Moratuwa, Sri Lanka, in 2007. He is currently working toward the Ph.D. degree in electrical and electronic engineering at the University of Auckland, Auckland, New Zealand.

From 2007 to 2012, he was an Electrical Engineer for ABB AG, Mannheim, Germany. His research interests include the areas of power electronics, inductive power transfer, and matrix converters.

Duleepa J. Thrimawithana (M'09) received the B.E. (first class Hons.) degree in electrical engineering and the Ph.D. degree in power electronics from the University of Auckland, Auckland, New Zealand, in 2005 and 2009, respectively.

From 2005 to 2008, he was, in collaboration with Tru-Test Ltd., Manukau, New Zealand, a Research Engineer in the areas of power converters and high-voltage pulse generator design. In 2008, he joined the Department of Electrical and Computer Engineering, the University of Auckland, as a part-time Lecturer, where he is currently a Senior Lecturer. His main research interests include the fields of inductive power transfer, power electronics, and renewable energy.

Udaya K. Madawala (M'95–SM'06) received the Graduate degree with B.Sc. (Hons.) degree in electrical engineering from The University of Moratuwa, Moratuwa, Sri Lanka, in 1987, and the Ph.D. in power electronics from The University of Auckland, Auckland, New Zealand, in 1993.

After working in industry, he joined the Department of Electrical and Computer Engineering, The University of Auckland as a Research Fellow in 1997. He is currently an Associate Professor, and his research interests include the fields of power electronics, inductive power transfer, and renewable energy.

Dr. Madawala as an active IEEE volunteer, serves as an Associate Editor for the IEEE TRANSACTIONS ON INDUSTRIAL ELECTRONICS and the IEEE TRANSACTIONS ON POWER ELECTRONICS. He is a Member of the Power Electronics Technical Committee of Industrial Electronics Society and the Sustainable Energy Systems Committee of IEEE Power Electronics Society.